

The radiative response of solar loop plasma subject to transient heating^{*}

S. J. Bradshaw and H. E. Mason

Department of Applied Mathematics and Theoretical Physics, Centre for Mathematical Sciences, University of Cambridge, Wilberforce Road, Cambridge CB3 0WA, UK

Received 7 april 2003 / Accepted 17 June 2003

Abstract. In Bradshaw & Mason (2003) we carried out a hydrodynamic simulation of a cooling solar loop and investigated the nonequilibrium response of the population of C VII ions to the changing conditions in the plasma. We also compared equilibrium and nonequilibrium calculations of the total plasma emissivity. In this paper we present two simulations of a solar loop subject to a transient heating process delivering energy on the nanoflare scale at its apex. One simulation treats the ion populations and the energy radiated from the loop plasma entirely as though the system were in equilibrium and the other simulation performs a full nonequilibrium treatment by coupling the time-dependent ion populations to the hydrodynamic equations through the radiative energy loss. Our radiative model accounts for the 15 most abundant elements of the solar atmosphere including C, O, Ne, Mg, Si and Fe.

We find some pronounced differences between the populations of certain transition region ions and the corresponding plasma emissivity curves in the equilibrium and nonequilibrium simulations. Though the apex heating event is relatively weak in comparison to energy released on the microflare and flare scales, nonetheless a significant amount of energy reaches the loop footpoint region to heat the plasma there and we find a nonequilibrium spike in emissivity. However, more surprisingly we find considerable differences between some of the coronal ions in the equilibrium and nonequilibrium simulations, with important consequences for the plasma emissivity curves. In particular, we find that the total plasma emissivity calculated assuming equilibrium conditions is up to a factor of 5 lower than the nonequilibrium emissivity and this is due almost entirely to the response of the coronal Fe ions.

Finally, we suggest possible observational signatures of nonequilibrium ionisation and ways in which one might identify it. This is important because an invalid assumption of equilibrium ion populations may well lead one to incorrect conclusions about the properties of the plasma in both a broad-band and narrow-band/emission line based analysis.

Key words. Sun: transition region – Sun: corona – plasmas – hydrodynamics

1. Introduction

In our previous work (Bradshaw & Mason 2003, hereafter referred to as BM) we introduced a hydrodynamic model of a cooling solar loop with a fully time-dependent treatment of the ion populations and the radiative energy loss from the loop plasma. We focused upon the population of C VII in our analysis for two reasons: (a) because it nicely emphasises the effect we wish to draw attention to and (b) because of the consequences the nonequilibrium effect on C VII has for the more weakly ionised states of C that are very important transition region emitters. We also showed a comparison between the total plasma emissivity ($\text{erg cm}^{-3} \text{s}^{-1}$) calculated under conditions of equilibrium and nonequilibrium. We found that the transition region emission is greatly reduced under nonequilibrium conditions as the loop plasma cools.

Send offprint requests to: S. J. Bradshaw,
e-mail: S.J.Bradshaw@damtp.cam.ac.uk

^{*} Figures 11 to 13 and Appendix A are only available in electronic form at <http://www.edpsciences.org>

We now turn our attention to the case of a heated loop and in particular we consider the case of a loop undergoing a transient heating process with energy delivered at its apex. One might envisage, for example, heating via reconnection with an overlying arcade of loops. However, we are not so concerned with the nature of the heating and its potential significance for the ongoing coronal heating debate, as we are with investigating the effect of a dynamic heating episode upon the ion populations of the loop plasma and consequently upon the total amount of energy radiated.

There are several precedents for carrying out this kind of work, which have highlighted the importance of considering the effects of nonequilibrium ionisation for the purposes of plasma diagnostics and theoretical modelling. A number of authors have carried out studies into the effects that a steady state flow can have on the ion populations. Dupree et al. (1979) investigated the effect of a flow on the ionisation state of plasma in the transition region and showed that the large temperature gradient combined with the flow can result in a departure from

ionisation equilibrium as the ions are carried into regions with temperatures different from their temperatures of peak abundance. Borrini & Noci (1982) investigated the ionisation conditions in coronal loops in the temperature range 0.2–2 MK and showed that considerable deviations from equilibrium ionisation can occur in loops of average or low intensity (or density) and characterised by high speed flows. This was reported to be especially true for cool loops, despite having somewhat lower velocities, because they were found to have larger (negative) density and temperature gradients than hot loops. Noci et al. (1989) calculated the number densities of carbon ions for a selection of loop models and found evidence of nonequilibrium ionisation effects for velocities of only a few km s^{-1} at the loop top and a factor of 10 less at the base, with densities in the range 10^8 to 10^{10} cm^{-3} . These results are in close agreement with those of BM under very similar conditions.

Spadaro et al. (1990) extended the work of Noci et al. by calculating the emissivity of the ions of carbon and oxygen for a set of coronal loop models, with and without the assumption of ionisation equilibrium, finding considerable differences between the radiative loss functions ($\Lambda(T)$) in each case and used the nonequilibrium radiative loss function to solve again the steady state flow equations of the loop models. They concluded that nonequilibrium ionisation induced by plasma flows in coronal loops can strongly alter the radiative loss function and found that for upflowing plasma (i.e. flowing up the temperature gradient) the radiative loss rate is enhanced. For downflowing plasma they found that the radiative losses are suppressed, another result in agreement with BM (cf. Figs. 7 & 9 of BM).

Other authors have investigated the response of an ion population to a strong heating event in time-dependent hydrodynamic models. The work of MacNeice et al. (1984) in calculating the departure from equilibrium of calcium ions during a solar flare is discussed in BM, as are the more recent papers of Erdélyi et al. (1998), Erdélyi & Sarro (1999) and Sarro et al. (1999) describing their work on UV transition region transients (microflares, explosive events or blinkers) and the red-shift/blue-shift problem of transition region flows.

There have also been a number of studies to determine the effects that nonequilibrium ion populations might have on the information derived from observables. In particular, plasma properties such as temperature, density and emission measure, commonly calculated using the techniques of spectroscopic diagnostics (see Mason & Monsignori Fossi 1994, for a review) applied to spectral lines observed by the CDS and SUMER instruments onboard the SOHO satellite, are heavily dependent upon the relative populations of the emitting ions (see also Sarro et al. 1999). Teriaca et al. (1999a,b) have considered nonequilibrium ionisation as a means to explain the nature of the emission spectrum associated with the red-shift/blue-shift problem mentioned above. They explore the possibility that a nanoflare occurring at the O VI formation temperature can explain the observed red-shift of transition region lines and the blue-shift of high transition region/low coronal lines. By converting the temporal evolution of the thermodynamic state of the loop plasma into line profiles in nonequilibrium ionisation

they were able to derive magnitudes for the red and blue shifts in reasonable agreement with observations.

Doschek & Tanaka (1987) considered the effects of a transiently ionising solar flare plasma on the X-ray spectrum of iron. They found some evidence of transient ionisation in flare spectra obtained from the SOX 1 spectrometer on the Japanese Hinotori spacecraft and considered the importance of transient effects in deriving information from the upflowing plasma associated with chromospheric evaporation. Edgar & Esser (2000) have examined the accuracy of a common first ionisation potential (FIP) effect diagnostic, the ratio of Ne VI to Mg VI lines in the transition region, subject to a number of simple flows. By calculating spectral line ratios they demonstrate that in addition to temperature dependence, nonequilibrium effects must be taken account of for each line ratio used in the diagnostic.

There are compelling reasons to consider nonequilibrium ion populations for a variety of solar phenomena in terms of both observational and theoretical work. Furthermore, one should also consider the implications that a nonequilibrium ion population has for the energy balance of solar loop plasma via radiative emission, given that the energy balance provides a vital characteristic through which we hope to derive much information and an understanding of the nature of solar loops. For example, the popular scaling laws of Serio et al. (1981) were derived through the assumption that radiative emission can be taken to be in equilibrium.

The current paper is divided into 4 sections. In Sect. 2 we describe the hydrodynamic and radiative models, and give details about the simulations that were performed. In Sect. 3 we present the results from the simulations and discuss them. In Sect. 4 we present our conclusions and plans for future work.

2. Hydrodynamic and optically thin radiative modelling

We used the same hydrodynamic code as in BM to perform the simulations described in this paper with two important developments. Following the work of Betta et al. (1997), Reale et al. (2000) and the earlier work of MacNeice (1986), who demonstrate the importance of adequately resolving the transition region when attempting to accurately model the plasma dynamics, we introduce an adaptive regridding scheme into our code in order to ensure that the steep transition region gradients are correctly resolved. Failure to achieve adequate spatial resolution in the transition region results in an underestimation of the gradients and consequently the incorrect calculation of the conductive flux from the corona into the chromosphere.

In BM the transition region moved away from the high resolution regions of the fixed grid (where it was well resolved at $t = 0$) as the loop cooled and it became under resolved at later times. However, given that the effect of under resolution is to underestimate the magnitude of the gradients involved then the actual effect of nonequilibrium ionisation in the transition region especially, should be even more significant than we demonstrated. The adaptive regridding scheme developed for our hydrodynamic code is based upon that described by Betta et al. but generalised to the case of asymmetric loop evolution as in Reale et al. We find that this scheme

is extremely effective in resolving the transition region as it moves rapidly towards the loop base and we are able to satisfy the dual requirements of minimising the cell-to-cell variation in the physical variables T , P and n (temperature, pressure and number density, respectively) and minimising the variation in cell width in order to preserve the order of the spatial derivatives. In Appendix A we present an analysis of the suitability of our code to hydrodynamic problems of the kind we are interested in. This is achieved through a series of tests designed to assess its stability and accuracy.

The solution of the time-dependent ionisation balance equations coupled to the time-dependent hydrodynamic equations for a realistic model solar atmosphere represents a major computational challenge. We include 144 ions in our model and so the total number of equations to be solved in each cell of the computational grid is 147 (144 plus the three hydrodynamic equations). Typically there are around 700 grid cells per time step in our simulations and therefore a total of just over 100 000 equations to be integrated. The method of integration we use is 2nd order accurate in time and so in actuality over 200 000 equations are solved to advance the solution by a single time-step. Due to the relatively small time-scales that can be encountered during impulsive heating events and the correspondingly small time-steps required for numerical stability, the hydrodynamic code has been parallelised using the MPI system and a worthwhile speed increase for the programming effort involved was obtained.

We construct our initial grid in exactly the same way as described in BM and in fact our initial atmosphere in the present work has almost identical properties. In summary: we adopt a curvilinear coordinate system where s is the position along the loop in the direction of the magnetic field and we set $T = 20\,000$ K at $s = 1500$ km. We set the conductive flux at $s = 1500$ km to zero and integrate the hydrostatic equations between $s = 1500$ km and the loop apex at $s = 40\,000$ km in order to derive the temperature and pressure profiles. We obtain a peak temperature at the loop apex of about 1.5 MK. An isothermal chromospheric layer at $T = 20\,000$ K is added to the loop between $s = 0$ and $s = 1500$ km by solving the hydrostatic pressure equation for constant T . The profiles are then mirrored about the loop apex under the assumption of apex symmetry (hence the conductive flux is also zero at the apex) to derive the profiles between $s = 0$ and $s = 80\,000$ km (the total length of the loop). We achieve the desired spatial resolution at $t = 0$ by limiting the step-by-step fractional variation in the physical quantities T , P and n to a maximum of 0.1. The coronal resolution is on the order of 100 km and the transition region resolution is on the order of 100 m.

When the initial static equilibrium atmosphere has been calculated the characteristic variables of temperature and pressure, defined at the cell edges, are converted into the conserved variables of mass density, momentum density (zero at $t = 0$) and internal energy density, which are then interpolated back onto the initial non-uniform grid in the cell centres. As a result of this process there is no longer a perfect balance of the forces and energy fluxes. Therefore, we adopt the approach of Klimchuk et al. (1987) by treating these imperfections as small amplitude perturbations and allow them to evolve. They

merely comprise background numerical noise on the order of 100 m s^{-1} and less, several orders of magnitude smaller than the sound speed, and consequently have no effect upon the evolution of the plasma when it is held in equilibrium (see Appendix A). For the case considered in the current paper these perturbations quickly become swamped by the large scale flows that develop as a result of the apex heating.

We solve the one dimensional, conservative form of the hydrodynamic equations in curvilinear coordinates (taken along the loop in the direction of the magnetic field):

$$\frac{\partial \rho}{\partial t} + \frac{\partial}{\partial s}(\rho v) = 0, \quad (1)$$

$$\frac{\partial}{\partial t}(\rho v) + \frac{\partial}{\partial s}(\rho v^2) = \rho g_{\parallel} - \frac{\partial P}{\partial s}, \quad (2)$$

$$\frac{\partial E}{\partial t} + \frac{\partial}{\partial s}[(E + P)v] = \rho v g_{\parallel} + \frac{\partial}{\partial s}\left(\kappa T^{5/2} \frac{\partial T}{\partial s}\right) + E_{\text{H}}(s, t) - E_{\text{R}}(s, t), \quad (3)$$

$$E = \frac{1}{2}\rho v^2 + \frac{3}{2}k_{\text{B}}nT, \quad (4)$$

$$P = 2k_{\text{B}}nT. \quad (5)$$

Here ρ , v , P and T are the mass density, bulk velocity, total pressure and temperature, respectively; g_{\parallel} is the gravitational acceleration parallel to the magnetic field; k_{B} is the Boltzmann constant; κ is the Spitzer coefficient of thermal conductivity and has a value of $9.2 \times 10^{-7} \text{ ergs cm}^{-1} \text{ s}^{-1} \text{ K}^{-7/2}$; E_{H} is the volumetric heating rate; and E_{R} is the energy loss rate due to radiation. Note that E_{R} is now a function of s and t and accounts for departures from ionisation equilibrium of the population of emitting ions.

The volumetric heating rate adopts the following form:

$$E_{\text{H}} = E_{\text{Hbg}} + E_{\text{H0}} \exp\left(-\frac{|s - s_0|}{s_{\text{H}}}\right) \sin\left(\pi \frac{t - t_0}{\tau_{\text{H}}}\right). \quad (6)$$

Here E_{Hbg} and E_{H0} are the background heat input required to maintain the initial atmosphere and the maximum transient heat input. The exponential term describes the spatial distribution of heat, where s_0 and s_{H} are the location of maximum heating and the heating scale length (or e-folding length). The sinusoidal term describes the transient behaviour of the heating pulse, where t_0 and τ_{H} are the onset time and the period (i.e. the time taken for it to rise, reach its maximum and decay).

The hydrodynamic equations are solved using the same boundary conditions described in BM and commonly adopted by other authors (Klimchuk et al. 1987; Spadaro et al. 2002, 2003).

We perform two simulations, beginning with our initial loop atmosphere and perturbing it using the following values for the parameters of the heating function:

$$E_{\text{Hbg}} = 2.4 \times 10^{-4} \text{ erg cm}^{-3} \text{ s}^{-1}, \quad E_{\text{H0}} = 0.1 \text{ erg cm}^{-3} \text{ s}^{-1}, \\ s_0 = 4 \times 10^9 \text{ cm}, \quad s_{\text{H}} = 1 \times 10^8 \text{ cm}, \quad t_0 = 0 \text{ s}, \quad \tau_{\text{H}} = 30 \text{ s}.$$

The above parameter values describe a heating pulse delivered symmetrically about the loop apex, with a maximum heat

input of $0.1 \text{ erg cm}^{-3} \text{ s}^{-1}$, a spatial scale of 10^8 cm (1000 km) and a period of 30 s. Only one pulse is delivered to the loop in each simulation and so only constant background heating remains after 30 s.

The amount of heat delivered to the loop by the pulse is about 10^8 erg cm^{-2} . The properties of the pulse are therefore very similar in terms of spatial and temporal characteristics, and the total energy delivered, to the properties of the typical nanoflare model described by Parker (1988). However, we emphasise again that we are not so concerned with the nature of the heating as we are with investigating the effect of a dynamic heating episode upon the ion populations of the loop plasma and consequently upon the total amount of energy radiated. One may easily infer from the details of our simulations, the characteristic properties of our loop plasma and from our results the likely significance of nonequilibrium ionisation and radiative emission for their own observations and theoretical models. Our aim is to present a physically reasonable scenario and to pursue its consequences.

The one and only difference between the two simulations is that one of them assumes the ion populations and the radiative losses remain in equilibrium (hereafter referred to as simulation A) and the other performs a fully time-dependent treatment of the ion populations and the radiative losses (hereafter referred to as simulation B). The equilibrium ion balances are calculated using the same ionisation and recombination rates as those used in the time-dependent ion balance equation. We adopt the rates of Mazzotta et al. (1998) calculated as functions of temperature in the low density limit and valid in the present case because of the relatively narrow range of densities (10^8 to 10^{10} cm^{-3}) encountered during the simulations. There has been some renewed interest recently in the density dependence of dielectronic recombination (Del-Zanna & Mason 2003), which can be shown to have a significant effect upon both the temperature of peak ion abundance and the magnitude of the peak abundance itself. The elemental abundances are those due to Feldman (1992) with a high coronal metallicity to take account of the FIP effect. The ion emissivities (the sum of the emission from each individual line of the ion) are calculated using the latest version of the CHIANTI atomic database (Young et al. 2003) as a function of temperature and density.

We assume that the fifteen most abundant elements of the solar atmosphere are sufficient by themselves to provide a physically reasonable and accurate calculation of the total radiative energy loss. Our radiative model incorporates every ion of these elements for which CHIANTI contains emissivity data, providing excellent ion coverage. The only potentially important ions missing from CHIANTI are those of neutral carbon and oxygen, which emit strongly at temperatures below those characteristic of our present work. Moreover our simulations do not reach temperatures hot enough to necessitate the inclusion of continuum emission, although a suitable (albeit equilibrium) treatment is also available from CHIANTI.

Thus, we calculate the emissivity for a single element (Y) in every grid cell as follows:

$$\Lambda_Y = 0.83 \times Ab(Y) \times \sum_{i=1}^{Z+1} Y_i \times \varepsilon_i. \quad (7)$$

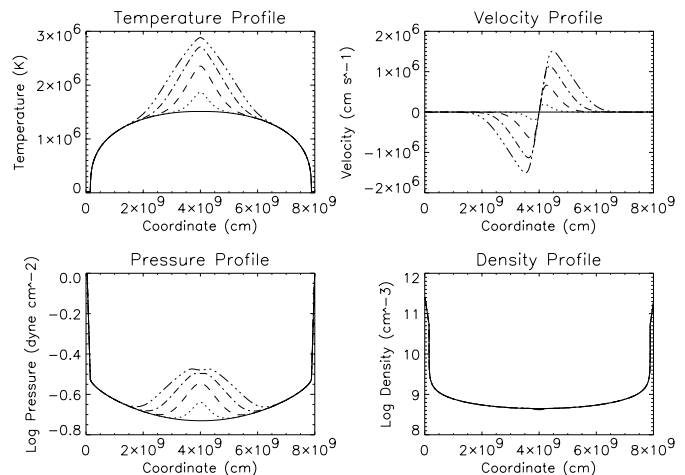


Fig. 1. Time series of the temperature, velocity, pressure and density at: 0 s (solid line), 5 s (dotted), 10 s (dashed), 15 s (dash-dot), 20 s (dash-dot-dot-dot). The flow velocity is always taken to be positive when it is in the direction of increasing curvilinear coordinate and this applies to all subsequent plots in which the velocity is included.

Λ_Y is measured in units of $\text{erg cm}^3 \text{ s}^{-1}$; 0.83 is the proton/electron ratio; $Ab(Y)$ is the abundance of element Y relative to hydrogen; the summation term is expressed assuming spectroscopic notation, where $Y_{i=1}$ is neutral Y (or YI), and sums the product of the ion population fraction (Y_i) and the total line emission (ε_i) for each ion; Z is the atomic number of the element.

For simulation A the values of Y_i are obtained by interpolation from a table of pre-calculated equilibrium values. For simulation B the values of Y_i are obtained by solving the following time-dependent ion balance equation for each ion:

$$\frac{\partial Y_i}{\partial t} + \frac{\partial}{\partial s} (Y_i v) = n (I_{i-1} Y_{i-1} + R_i Y_{i+1} - I_i Y_i - R_{i-1} Y_i). \quad (8)$$

Y_i denotes the fractional population (normalised to 1) of ion stage i of element Y ; the coefficients I_i and R_i are the ionisation and recombination rates from/to ion stage i ; n is the number density. The initial ($t = 0$) values of Y_i are obtained from the pre-calculated table of equilibrium values (see Fig. 3 of BM for an equilibrium ionisation balance of carbon). Therefore, by using these methods we are able to calculate the equilibrium and the nonequilibrium ion populations for all of the elements in every grid cell.

The total emissivity in every grid cell is then calculated by simply summing each of the Λ_Y for the elements included in the radiative model. The total radiative energy loss as a function of position (and therefore temperature) along the loop is then $E_R = n^2 \Lambda(T(s))$ in the case of simulation A and $E_R = n^2 \Lambda(T(s), t)$ in the case of simulation B.

3. Discussion of theoretical results

At $t = 0$ the heating pulse is switched on and there follows a very rapid and localised increase in the temperature and pressure of the loop about its apex. Figure 1 shows the evolution of the thermodynamic variables from footpoint to footpoint along the loop during the first 20 s of the pulse for simulation B.

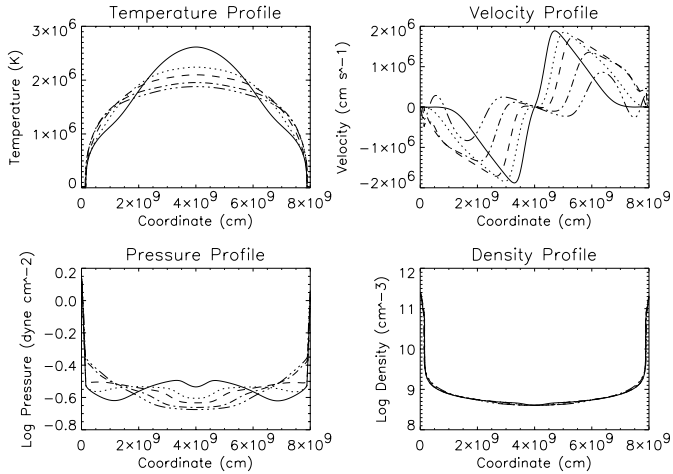


Fig. 2. Time series of the temperature, velocity, pressure and density at: 30 s (solid line), 45 s (dotted), 60 s (dashed), 90 s (dash-dot), 120 s (dash-dot-dot-dot).

Figure 2 plots their evolution from 30 s (after all of the energy from the heating pulse has been delivered) up to 120 s.

The temperature increases from approximately 1.5 MK to almost 3 MK at the loop apex in the first 20 s. At the same time the coronal pressure reaches a new maximum of about $0.35 \text{ dyne cm}^{-2}$ at the apex from an initial ($t = 0$) value of $0.19 \text{ dyne cm}^{-2}$. The steep rise in apex temperature creates conduction fronts that propagate towards the footpoints. The pressure gradients that develop as a result of the new pressure maximum at the apex drive flows and pressure waves towards the footpoints. The flow velocity reaches a peak value of 20 km s^{-1} after the first 30 s of loop evolution. The flows do not carry much mass away with them as shown in Fig. 1 by the almost imperceptible decrease in density at the apex.

There are no discernible differences between the thermodynamic profiles of simulations A and B during the 30 s heating pulse because the magnitude of the heat input, which reaches a peak on the order of $0.1 \text{ erg cm}^{-3} \text{ s}^{-1}$ at 15 s, is much larger overall than the magnitude of the radiative energy losses, which are on the order of $10^{-5} \text{ erg cm}^{-3} \text{ s}^{-1}$. The thermodynamics of the loop in both simulations are initially dominated by heating and by the thermal conduction arising as a result of the steep gradients on either side of the apex temperature maximum. The amount of energy transported away by the flows that develop symmetrically about the apex is an order of magnitude less than the heat input and thermal conduction.

However, by taking account of departures from equilibrium of the emitting ion population we will see that the characteristic emissivity profile in the apex region is significantly different to that which would be found for an equilibrium ion population. In fact, the radiative energy loss in simulation B is about a factor of 5 greater than in simulation A in the apex region (Fig. 8 and also Sect. 3.3). This is significant because it will affect the evolution of the loop after the heating event as it cools and the temperature gradients associated with the conduction fronts propagate away from the apex region. Clearly an even stronger heating event such as an X class flare would cause the plasma to reach even higher temperatures, with potentially larger

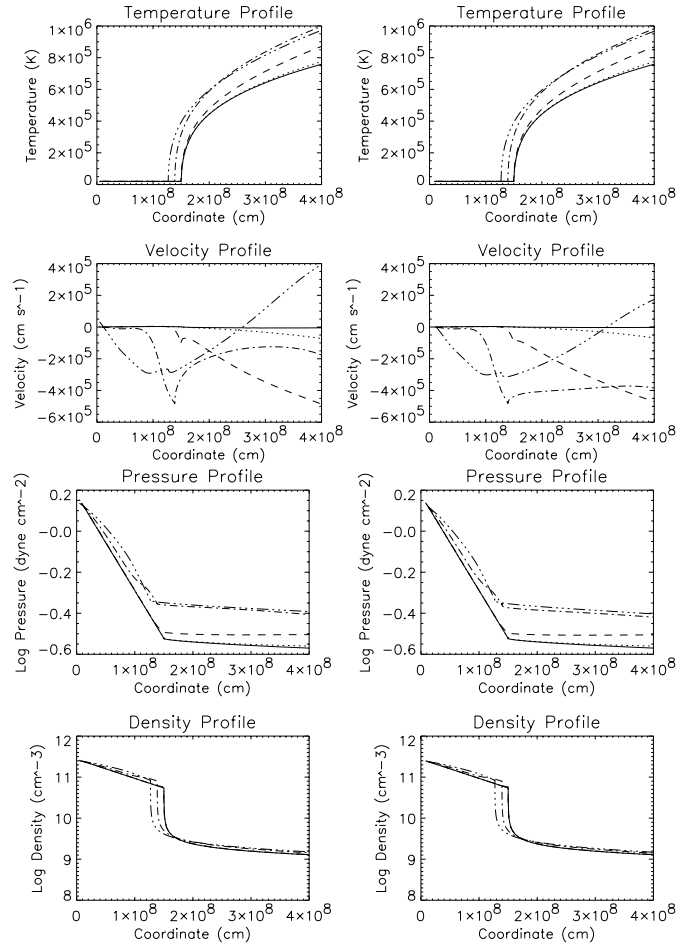


Fig. 3. Time series of the temperature, velocity, pressure and density in the footpoint region for simulation A (left column) and simulation B (right column) at: 30 s (solid line), 45 s (dotted), 60 s (dashed), 90 s (dash-dot), 120 s (dash-dot-dot-dot).

departures from equilibrium of the ion populations than are evident here, and the observed flare cooling curve (the rate of change of temperature with respect to time as the plasma cools) could only be explained by nonequilibrium radiative cooling.

Furthermore, the coronal emission is dominated by Fe and a broadband instrument designed to detect emission from Fe across a wide range of temperatures might easily miss a heating event such as the one described in the current work, because the emission remains almost constant (Fig. 9), despite the factor of 2 increase in temperature. This is obviously of relevance when one is searching for evidence of small-scale heating events such as nanoflares as it seems unlikely that a broadband instrument would have sufficient temperature discrimination to identify them.

After 30 s the apex plasma begins to cool from its new maximum and the conduction fronts continue to heat the plasma lower down as they travel towards the chromosphere. Figure 3 plots the evolution of the footpoint plasma from 30 s to 120 s. Since the simulation produces results that are symmetric about the apex we choose the left-hand footpoint for all subsequent footpoint analysis.

For the first 45 s there are no changes in the thermodynamic variables in Fig. 3 because the coronal disturbances that arise due to the heating pulse haven't yet reached the footpoints. There are some tiny fluctuations in the velocity profile (on the order of 50 m s^{-1}), but clearly these have absolutely no influence upon the evolution of the plasma. Indeed, the ability of the hydrodynamic code to hold the footpoint region of the loop in its initial static equilibrium configuration is a good indication of the stability of the code and its accuracy in resolving the large gradients and the large changes in gradient of the thermodynamic variables in the transition region (see Appendix A).

After 60 s we see in Fig. 3 that the conduction front reaches the upper transition region and begins to heat it. During the next minute the transition region moves further down the loop as chromospheric material is heated to transition region temperatures. The pressure of the region through which the transition region moves increases and its density decreases. The material from this region is pushed deeper into the chromosphere and we see a slight increase in the density lower down. We expect that a larger scale version of this effect accounts for the flashes that are observed during flares as a result of the compression of chromospheric material.

By comparing the velocity profiles in Fig. 3 it is evident that at 30 s, 45 s and 60 s they are in close agreement in the chromosphere/lower transition region in simulations A and B. However, at 90 s and 120 s there are some interesting differences that must arise due to the ways in which the radiative emission is handled. At 90 s the plasma velocity above 1500 km in simulation A is about a factor of two smaller towards the footpoint than in simulation B. Therefore, the downflows along the steep transition region gradients are larger in simulation B and though their magnitude is only about 4 km s^{-1} this should still be sufficient to transport a substantial amount of plasma between regions of considerable variation in temperature during the characteristic lifetimes of the important ions at those temperatures. Indeed, this is a feasible explanation for the nonequilibrium enhancement of C IV at 90 s in Fig. 5 and discussed in Sect. 3.1.

At 120 s we see in Fig. 3 that the velocity has become positive above 2600 km in simulation A and therefore the plasma is flowing towards the apex of the loop. In simulation B the velocity turns positive above 3000 km. The upwards directed velocities correspond to the ablation of lower-transition region and eventually chromospheric material as it is heated by the conduction fronts in exactly the same way as is predicted to happen in flares, though it occurs on a somewhat smaller scale in the simulations presented here and results in only a very slight density enhancement. The ablation is predicted to start sooner in simulation A than in simulation B and it reaches higher overall velocities in simulation A.

Another interesting point concerning this relatively small-scale ablation of material is that due to the conservation of momentum there must be an oppositely directed flow towards the footpoints and this is seen to be the case in Fig. 3 at 120 s. The cross-over point in the flow velocity from negative to positive is in the right temperature region to explain the commonly observed red-shifts in lower transition region emission lines and blue-shifts in upper transition region and coronal

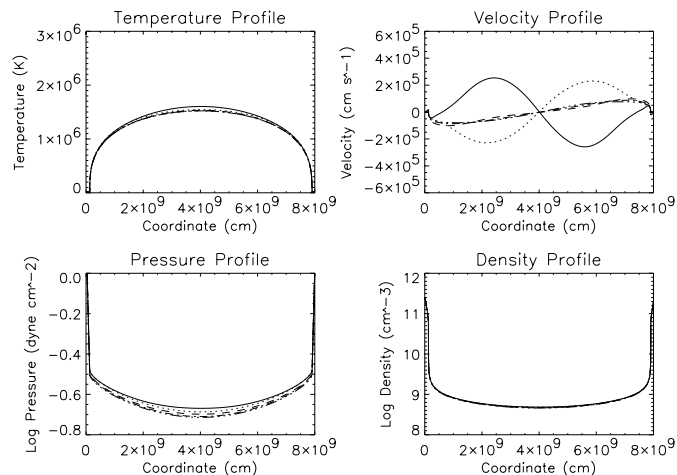


Fig. 4. Time series of the temperature, velocity, pressure and density at: 12 min (solid line), 15 min (dotted), 20 min (dashed), 25 min (dash-dot), 30 min (dash-dot-dot-dot).

emission lines. Teriaca & Doyle (2001) found red-shifts of 8.5, 6.1 and 1.7 km s^{-1} in spectral lines from C III, C IV and O V, and blue-shifts of 1.8, 3.9 and 10.7 km s^{-1} in spectral lines from O VI, Ne VII and Ne VIII respectively and suggested that the occurrence of a nanoflare at $T > 6 \times 10^5 \text{ K}$ might explain their results. The velocity values in Fig. 3 at 120 s in the footpoint region agree quite well with the lower range of Teriaca and Doyle's velocities, thus supporting the idea of a heating event at nanoflare energies giving rise to line shifts of the observed magnitude. However, the simulations show that the oppositely directed flows can arise as a result of the ablation of material and the conservation of momentum, and the nanoflare need not occur at transition region temperatures, which supports the theory of Parker (1988) that nanoflares occur in the corona. Therefore, red-shifts and blue-shifts can be explained as a natural consequence of a spatially localised and transient heating event, such as a nanoflare, occurring in the corona.

Figures 2 and 3 show that at around 120 s the pressure wave associated with the flow has been reflected from the transition region/chromosphere boundary, due to the large changes in gradient encountered, and propagates back towards the loop apex. At subsequent times the pressure wave is reflected back and forth between the apex and footpoint, gradually decaying as the flow velocities are reduced and the loop returns to its initial equilibrium configuration.

After half an hour of evolution from the onset of the heating pulse Fig. 4 shows that the loop has more or less returned to its $t = 0$ equilibrium configuration. There are no significant changes in the thermodynamic variables between 12 and 30 min, and the velocity profile decays from peak values of about 3 km s^{-1} at $s = 2 \times 10^9 \text{ cm}$ to negligible values in the corona and values on the order of 0.1 km s^{-1} in the upper transition region at $s \approx 5 \times 10^8 \text{ cm}$. The ability of the hydrocode to recover the initial equilibrium is another good indication of its stability and accuracy.

We have described the morphology of the loop plasma in terms of the thermodynamic variables: temperature, pressure, density and velocity, in response to the heating pulse located

Table 1. Temperatures of peak abundance for the selected transition region ions.

Ion	$\text{Log}_{10} T_{\text{peak}}$
C IV	5.0
O V	5.4
Ne VIII	5.8
Mg IX	6.0

at the apex. Figures 1 through 4 show the spatial and temporal evolution of the loop plasma from footpoint to footpoint, and enlarged views of the left-hand footpoint alone. We now turn our attention to the populations of some important transition region and coronal ions, and consider the ways in which nonequilibrium processes affect their relative abundances and consequently the total amount of energy radiated by the plasma.

3.1. Transition region ion populations

The transition region ions we have chosen to highlight the effects of nonequilibrium ionisation are C IV, O V, Ne VIII and Mg IX. The temperatures of peak abundance (in equilibrium) of these ions are given in Table 1. The choice of these ions is not arbitrary, rather, they have been selected because they emit important spectral lines that are used in spectroscopic diagnostics to calculate plasma temperatures, densities and line shifts.

Sarro et al. (1999) and Teriaca et al. (1999a,b) red-shifted component of observed transition region flows. They simulated an explosive event located at a loop footpoint and calculated the magnitude of the red-shift in the C IV line profiles in an attempt to explain the presence of such flows. Observational tests for nonequilibrium ionisation due to flows in the transition region have been suggested by Spadaro et al. (1994a,b) using the temperature sensitive line ratios of C IV [1548/312] and O V [629/172]. O V also emits lines that are used by the SUMER instrument onboard SOHO for density diagnostics.

O’Shea et al. (2001) have studied active region oscillations using high cadence observations of lines emitted by O V and Mg IX. They find a persistent 5 min oscillation present in all lines as evidence of wave activity in the transition region. Mg IX is also useful for density diagnostics and in particular the Mg IX 368 Å line of the CDS (NIS) instrument onboard SOHO has been used extensively to study coronal holes (Mason & Monsignori Fossi 1994). Strong similarities exist between images seen in the TRACE 173 Å filter and CDS observations in Mg IX, confirming that the lines detected by each instrument at these wavelengths are emitted over the same temperature range (Del-Zanna & Mason 2003). Therefore, these are extremely useful wavelengths to use when attempting to correlate features present in CDS observations with those in the higher resolution TRACE images.

Ne VIII is used by the SUMER instrument to measure line-shifts and thus derive line-of-sight flow velocities. However, the theoretical and observed intensities of the line emission do not agree for this ion. The disparity between theory and

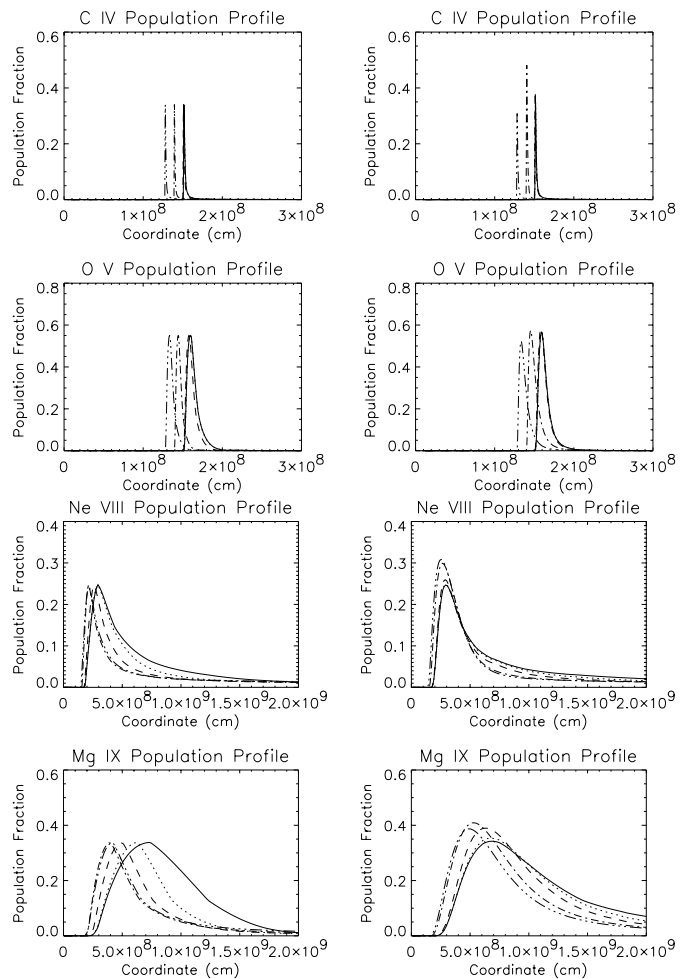


Fig. 5. Time series of the C IV, O V, Ne VIII and Mg IX population fractions for simulation A (left column) and simulation B (right column) at: 30 s (solid line), 45 s (dotted), 60 s (dashed), 90 s (dash-dot), 120 s (dash-dot-dot-dot).

observation can be as much as a factor of 2–3 and is probably due to incorrect values for the ion populations (Del-Zanna, private communication 2003). Ne VIII is one of the problematic Li-like ions for which a consideration of the density dependence of dielectronic recombination is likely to be important when calculating ionisation balances (Raymond, private communication 2001). Accounting for nonequilibrium ionisation might also conceivably help to bring theory into closer agreement with observation. Teriaca et al. (1999b) perform nonequilibrium ionisation calculations for Ne VIII to investigate the blue-shifted component of the transition region flows they study.

Figure 5 shows the population fractions of the four ions discussed above for simulations A and B between 30 s and 120 s as they respond to the conduction front reaching the transition region and the chromosphere. The most notable difference between the C IV profiles of simulations A and B is the significant enhancement in the population of C IV at 90 s followed by a reduction of similar magnitude at 120 s in simulation B, as the ionisation front moves with the transition region down

the loop. We discussed above the likely possibility that this enhancement in C IV is due to the presence of downflows carrying persistent C IV ions into regions of temperature lower than their typical formation temperature. The O V profiles do not exhibit significant differences between simulations A and B. There is a slight enhancement followed by a decrease in the O V population fraction in simulation B over that of simulation A, which becomes slightly more pronounced at later times than those shown in Fig. 5, though overall the differences are not as striking as those evident in the C IV profiles.

Ne VIII and Mg IX also exhibit the trend of enhanced ion populations in nonequilibrium ionisation. Figure 5 shows the population of Ne VIII and Mg IX from the footpoint region to about a quarter of the way along the loop. This covers the transition region and the lower part of the coronal segment.

At 30 s the conduction front has not quite reached the region of peak Ne VIII and Mg IX abundance and therefore the population maxima of both ions retain their magnitudes and positions. However, we do see a reduction in the ion populations on the right-hand wing of the curves at 30 s in simulation A (compared with simulation B) because the ions are assumed to respond immediately to the increase in temperature. In simulation B the curves at 60 s are still very close to the curves at 30 s because the finite amount of time the ions take to respond to the increase in temperature is accounted for.

Between 90 s and 120 s the populations of Ne VIII and Mg IX are considerably reduced on the right-hand wing of the curves in simulation A compared with simulation B, with differences of up to a factor 3. In addition, the magnitudes of the population maxima in simulation B increase as they move lower down the loop. This is due to the finite response time of the ions to the increase in temperature and a contribution from the enhanced overlying ion populations via transport processes. Overall in simulation B the population of Ne VIII and Mg IX are everywhere enhanced in comparison with simulation A.

This enhancement in ion populations when they are calculated in nonequilibrium ionisation is a feature of similar work and provides a means to explain the increase in emission commonly observed as a consequence of an explosive event. If the heating pulse occurred closer to the footpoint and/or the magnitude of the energy delivered was larger then one would expect this effect to be considerably more pronounced, particularly the initial enhancement in the ion populations. Sarro et al. model strong heating events at a loop footpoint and calculate almost a factor of 2 increase in the population of C IV in the nonequilibrium case compared with an equilibrium calculation.

At later times in our simulations the nonequilibrium populations of C IV and O V are considerably reduced, by up to factors of 2 for C IV and 1.5 for O V, from the corresponding equilibrium populations. This is significant and our previous work in BM suggests it is the persistent higher ionisation stages that dominate in the transition region as the loop gradually cools and returns to its initial equilibrium state. Therefore, after a strong heating event one might find a surprisingly large population of higher ionisation stages present in the footpoint region that can only be explained by a nonequilibrium treatment of the ion populations.

Table 2. Temperatures of peak abundance for the selected coronal ions.

Ion	$\text{Log}_{10} T_{\text{peak}}$
Fe IX	5.8
Fe X	6.0
Fe XII	6.1
Si XII	6.3

After about 10 min of loop evolution the population fractions of O V, Ne VIII and Mg IX are in close agreement between simulations A and B, and thereafter their nonequilibrium evolution follows their equilibrium evolution. After half an hour of loop evolution the populations of O V, Ne VIII and Mg IX in both simulations return to their initial equilibrium values. C IV, on the other hand, exhibits a nonequilibrium population reduced by a factor of about 1.3 from its corresponding equilibrium population, suggesting that higher ionisation stages of low charge elements could be present in footpoint regions for a relatively long time and should be detectable by instruments such as CDS. Observations of higher ionisation stages than would otherwise be expected in footpoint regions would be strong evidence for the presence of nonequilibrium ionisation processes.

3.2. Coronal ion populations

The coronal ions we have chosen to highlight the effects of nonequilibrium ionisation are Fe IX, Fe X, Fe XII and Si XII. The temperatures of peak abundance (in equilibrium) of these ions are given in Table 2. Emission lines from these ions are commonly used to study coronal plasma at temperatures around 1 MK and above. Fe IX and Fe X are the main contributors to the TRACE 171 Å filter and Fe XII is the main contributor to the TRACE 195 Å filter. Si XII is a good indication of the presence of very hot (2–3 MK) plasma since it is a strong emitter at high temperatures. The spectral coverage of CDS also includes emission from these ions and so once again they are important for joint CDS and TRACE observations of the type that have recently been carried out (Del-Zanna & Mason 2003) and are planned in the near future. It is an inarguable fact that spectral and imaging instruments are required to complement one another if we are to make progress with the major problems in present-day solar physics. It is also necessary to ensure that we understand the behaviour of the ions from which we draw our observational conclusions and these considerations underlie our choice of ions for the current study.

Figure 6 shows the population fractions of these four ions for simulations A and B during the first 20 s of evolution as the apex temperature rises sharply from 1.5 MK to 3 MK due to the heating pulse. It is immediately obvious from both simulations that we should not expect to see any emission from Fe IX and only a little emission from Fe X from the apex region of the loop at the range of temperatures encountered. The conduction fronts do not reach the lower corona in either of these figures

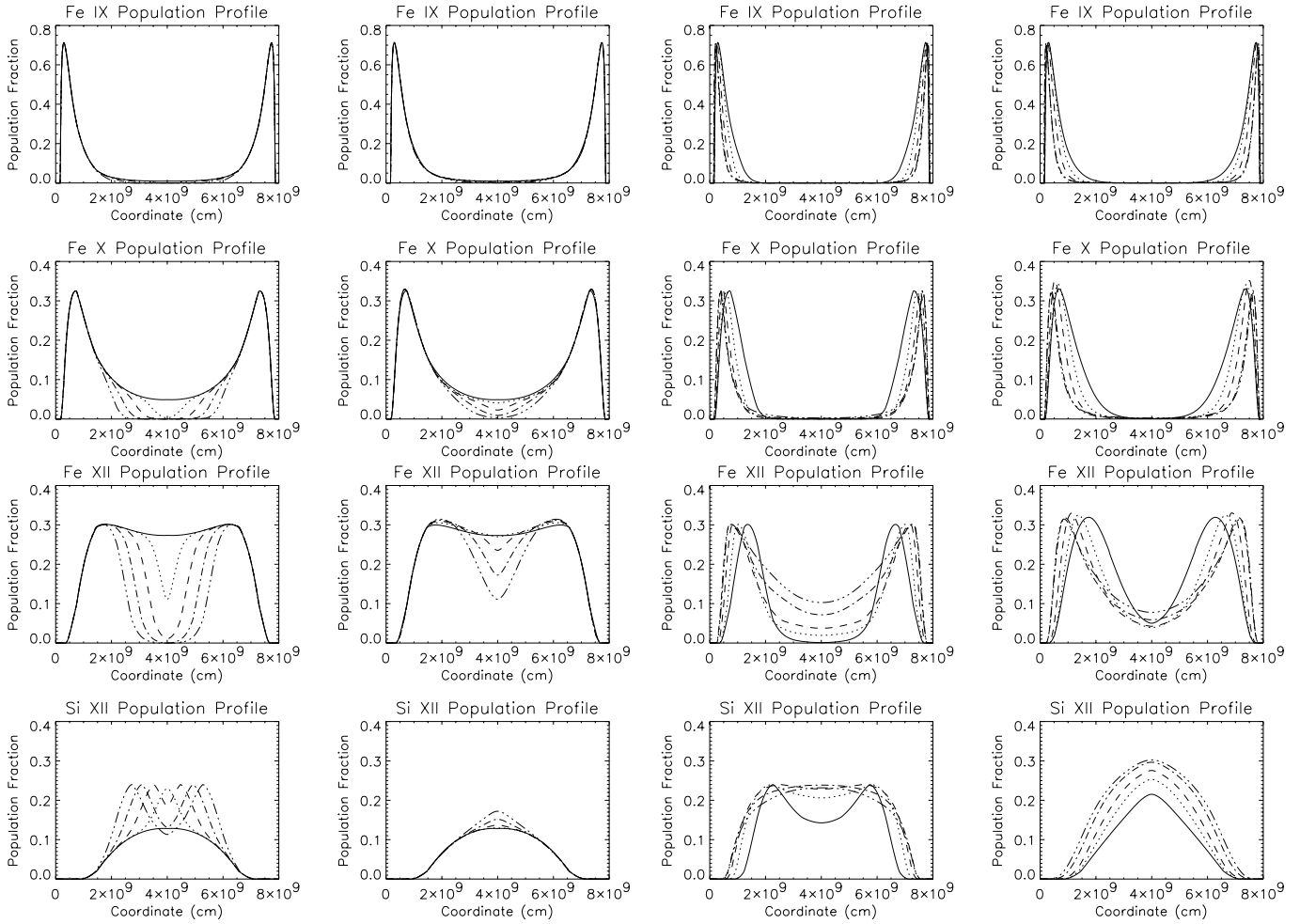


Fig. 6. Time series of the Fe IX, Fe X, Fe XII and Si XII population fractions for simulation A (left column) and simulation B (right column) at: 0 s (solid line), 5 s (dotted), 10 s (dashed), 15 s (dash-dot), 20 s (dash-dot-dot-dot).

Fig. 7. Time series of the Fe IX, Fe X, Fe XII and Si XII population fractions for simulation A (left column) and simulation B (right column) at: 30 s (solid line), 45 s (dotted), 60 s (dashed), 90 s (dash-dot), 120 s (dash-dot-dot-dot).

and so the fractional populations of Fe IX and Fe X at lower temperatures (around 1 MK and below) remain unchanged.

It is clear from Fig. 6 that simulations A and B tell very different stories in terms of the populations of Fe XII and Si XII. In simulation A we are led to believe that Fe XII vanishes entirely in the region of the loop apex as it reaches its maximum temperature after 20 s. In simulation B we see that the population of Fe XII is reduced to just below half of its initial value and remains a non-negligible presence. Furthermore, in the wings of the distribution either side of the apex in simulation B the population fraction of Fe XII actually increases because the nonequilibrium treatment allows for the transport of ions by the large flows that are seen in Fig. 1. Additionally, the lower ionisation stages that are present quickly ionise to Fe XII where the few seconds delay before ionisation to yet higher stages is sufficient to make the enhancement in the population of Fe XII appreciable.

In the case of Si XII, simulation A shows a rapid increase in its population at the apex for the first 5 s before ionisation to even higher stages begins to deplete it. After 20 s the population of Si XII has returned to almost the initial

population at the apex with considerable enhancements either side as lower stages are ionised to Si XII when the lower lying plasma is heated by the conduction fronts. Simulation B, however, is markedly different. Clearly Si XII does not respond quickly to the apex temperature increase and after the first 20 s there is only a modest increase in its population with correspondingly less ionisation to higher stages. Either side of the apex there is a factor of 2 less Si XII present than in the equilibrium calculation of simulation A. Our results indicate that were we to assume a state of equilibrium when interpreting observations containing emission from Si XII then we might underestimate the plasma temperature by not accounting for the fact that a significant amount of the ion can exist at temperatures far higher than the equilibrium calculation suggests.

Figure 7 shows the population fractions of Fe IX, Fe X, Fe XII and Si XII for simulations A and B between 30 s and 120 s as the loop evolves and the conduction fronts heat the transition region and the chromosphere. Again, there are no particularly significant differences in the Fe IX and Fe X profiles between simulations A and B at any time, and so the TRACE 171 Å filter represents equilibrium temperatures

under the kind of conditions encountered in our simulations. Of course, one should bear in mind that this might not necessarily be the case for even stronger heating in the region of peak Fe IX and Fe X abundance. The locations of peak Fe IX and Fe X population gradually move lower down the loop as the conduction fronts heat the plasma. The ionisation front due to Fe IX slightly leads that of Fe X, since Fe IX is ionised to Fe X as the local temperature increases with the passing of the conduction fronts and Fe X is in turn ionised to higher stages.

The population fractions of Fe XII and Si XII continue to exhibit important differences between simulations A and B as shown in Fig. 7. In simulation A Fe XII is fully depleted in the apex region at 30 s before being repopulated fairly quickly as the apex plasma cools between 30 s and 120 s. In simulation B a non-negligible amount of Fe XII remains in the apex region, but is repopulated more slowly during the initial phase of apex cooling. At later times the population fractions of Fe XII agree very closely between the two simulations suggesting that the characteristic lifetime of Fe XII is on the order of about 1 minute in the conditions encountered. The locations of peak Fe XII abundance are seen to move down the loop with the conduction fronts and the ionisation front due to Fe XII lagging behind that of Fe X, as expected.

In simulation A, Fig. 7 shows that Si XII is also repopulated fairly quickly after its initial depletion at the apex. There is no initial depletion in simulation B and the population of Si XII continues to increase, reaching a peak of about 0.3 in comparison with just less than 0.25 in simulation A. In both simulations the lower stages of Si are ionised to Si XII as the lower lying plasma is heated and the width of the Si XII profile along the loop increases, though this occurs considerably more slowly in simulation B due to the finite response time of the ions to the temperature increase. The differences in the Si XII profiles between the two simulations persist to later times, with a larger population fraction in the apex region and a smaller population fraction in the low corona in simulation B.

After about 10 min of loop evolution the population fractions of Fe XII and Si XII are in close agreement between simulations A and B, and thereafter their nonequilibrium evolution follows their equilibrium evolution. The characteristic lifetimes of Fe IX and Fe X are relatively short (on the order of 30 s or less) and so we don't expect to see much difference in their populations between simulations A and B. The fact that this is seen to be the case gives us confidence in our calculations when considerable differences between equilibrium and nonequilibrium ion populations emerge. Finally, after half an hour of loop evolution the initial equilibrium populations of these coronal ions are recovered.

3.3. Plasma emissivity

A number of authors such as those mentioned in previous sections have calculated nonequilibrium ion populations and found results in broad agreement with our own, though the physical processes studied may have been somewhat different than ours in terms of time-scales, total energy delivered and so

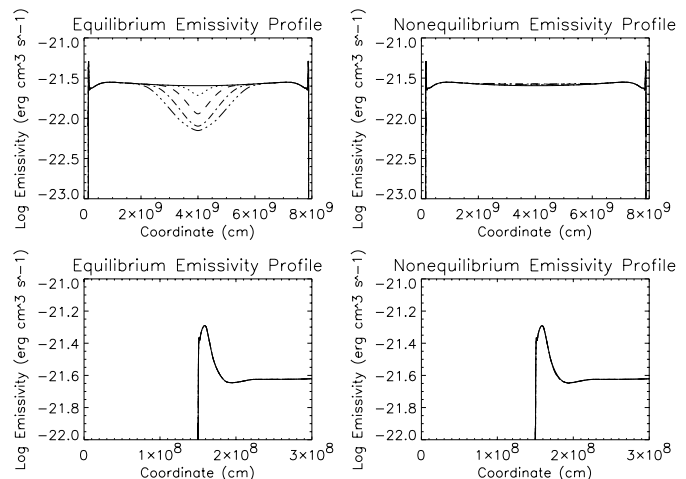


Fig. 8. Time series of the total emissivity in the coronal and footpoint regions of the loop for simulation A (left column) and simulation B (right column) at: 0 s (solid line), 5 s (dotted), 10 s (dashed), 15 s (dash-dot), 20 s (dash-dot-dot-dot).

on. In addition, several of these authors have calculated corrections to the usual equilibrium emissivity curve employed in optically thin radiation calculations for the solar atmosphere in order to allow for a nonequilibrium ion population. However, these corrections are applied in the post-processing of simulation results. One unique aspect of our work and the code we have developed is the ability to allow for the emissivity of a nonequilibrium ion population at each time-step of our simulations as they are being carried out and thus achieve a self-consistent approach to coupling the effects of a nonequilibrium ion population with the plasma hydrodynamics.

In BM we presented a comparison between plots of total emissivity calculated both in and out of equilibrium. We now take this a stage further and examine the individual contributions to the total emissivity from some important elements. Figure 8 shows plots of the total emissivity in the coronal and left-hand footpoint region of the loop during the first 20 s of loop evolution in equilibrium and nonequilibrium (simulations A and B, respectively). The dramatic difference in the coronal emissivity between simulations A and B is immediately apparent. During the heating event in simulation A the total emissivity rapidly decreases to about a factor of 5 less than its initial value. Conversely, in simulation B there actually appears to be a very slight increase in the total emissivity of the plasma during the same period and under the same conditions.

Figure 9 shows plots of emissivity for the elements Fe and Si, both in and out of equilibrium, during the first 20 s of loop evolution. The top two plots are the emissivity profiles from simulation A and the bottom two plots are those from simulation B. It is immediately obvious that the dominant contributor to the coronal emissivity is Fe and the evolution of the total emissivity of the coronal plasma in simulation A closely follows the evolution of the emissivity profile of Fe. In simulation A the large decrease in total plasma emissivity is accounted for by the substantial decrease in the emissivity of Fe. Similarly, the slight rise in total plasma emissivity in simulation B can be explained by the small decrease in the emissivity

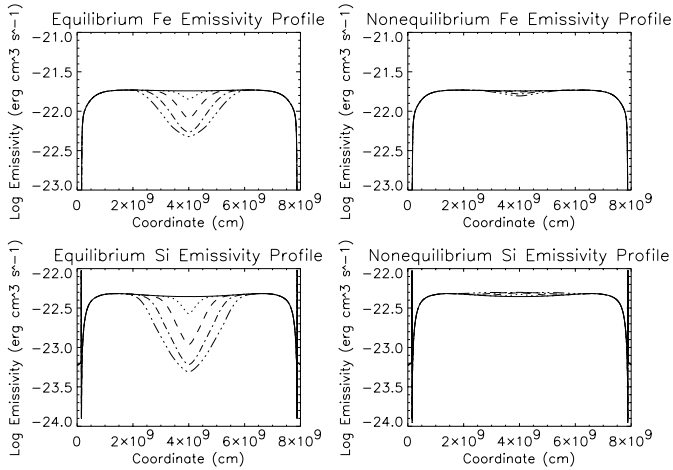


Fig. 9. Time series of the Fe and Si emissivity for simulation A (left column) and simulation B (right column) at: 0 s (solid line), 5 s (dotted), 10 s (dashed), 15 s (dash-dot), 20 s (dash-dot-dot-dot).

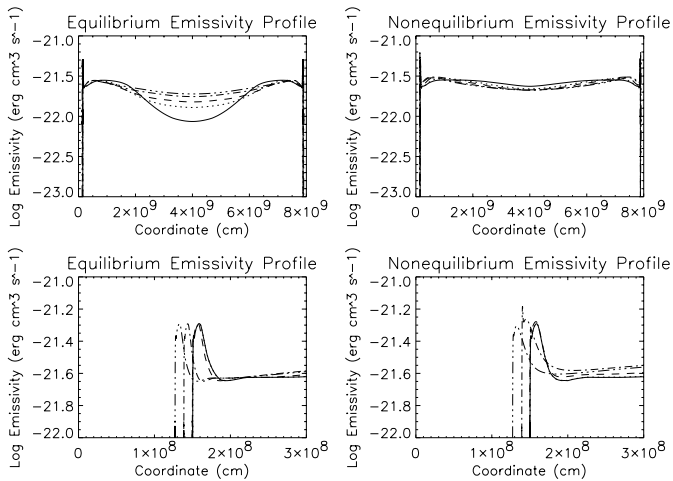


Fig. 10. Time series of the total emissivity in the coronal and footpoint regions of the loop for simulation A (left column) and simulation B (right column) at: 30 s (solid line), 45 s (dotted), 60 s (dashed), 90 s (dash-dot), 120 s (dash-dot-dot-dot).

of Fe which is countered by an increase in the emissivity of Si, Mg and the other coronal emitters whose ions have considerably longer characteristic lifetimes in the coronal plasma than those of Fe.

In Fig. 10 we provide plots of the total plasma emissivity in the coronal and left-hand footpoint regions of the loop as it evolves between 30 s and 120 s. The top two plots are the results from simulation A and the bottom two are those from simulation B. In the coronal region between 30 s and 120 s the total emissivity in simulation A increases, and by 120 s there are no discernible differences in the profiles of simulations A and B. In the footpoint region of simulation B there is a clear emission spike at 90 s as the plasma in the footpoint region responds to being heated by the conduction front. This spike is not present in simulation A and arises due to the effect observed in Fig. 5 whereby the populations of strong emitters such as C IV are seen to be enhanced in nonequilibrium conditions because of the presence of downflows. C IV reaches

its peak equilibrium population at $T = 10^5$ K and downflows carry C IV ions into lower temperature regions where they can persist for extended periods of time, thus resulting in a population enhancement. The subsequent depletion of C IV ions occurs when they are carried even further down the loop into the densest regions ($n > 10^{11} \text{ cm}^{-3}$) where they can quickly recombine.

4. Summary and conclusions

We have carried out two simulations of a solar loop subject to a perturbation at its apex, delivering approximately 10^8 erg cm^{-2} in a pulse with similar spatial and temporal characteristics to a typical nanoflare model. We have calculated the radiative response of the coronal and transition region plasma for equilibrium and nonequilibrium ion populations in a self-consistent way by coupling the system of time-dependent ionisation balance equations for all of the ions in our model atmosphere to the full set of time-dependent hydrodynamic equations. As in BM we include the 15 most abundant elements of the solar atmosphere in our model, comprising 144 ions in total for which CHIANTI provides emissivity data. Our computational code has been improved with the addition of an adaptive regridding scheme which ensures that the steep transition region gradients are adequately resolved at all times.

Our results have clear implications for the observation of transient heating events that may occur in the coronal plasma. We have seen that the apex temperature of the loop increases by a factor of 2 during the heating pulse and yet the emissivity, taking into account a nonequilibrium ion population, hardly changes (Figs. 8, 9). As a consequence a broad-band imaging instrument that covers a wide range of lines within a given temperature range may not be able to provide conclusive observational evidence for the occurrence of explosive heating events in the coronal plasma. This example highlights the need for high-resolution spectrometers in future space missions, capable of resolving the individual emission lines that do exhibit significant and measurable variations during transient heating events in low density plasma, such as SOLARB EIS. For example, in Fig. 6 we have seen that during the heating pulse the population of Fe XII changes sufficiently enough to have an observable effect upon the individual line emission, which ought to allow such an event to be observationally identified.

Indeed, one might conceivably use temporal variations in the ratio of observed populations of ion pairs as evidence of the presence of nonequilibrium ionisation. Any significant deviation from the predicted equilibrium ratio in the observed plasma conditions might act as a signature of nonequilibrium ionisation. A good choice of ion pairs to use to calculate the ratio would be those that are reasonably populous in the temperature range of interest and with substantially different characteristic lifetimes to one another. For example, it is clear in Fig. 5 that while the C IV population exhibits dramatic differences between simulations A and B, the O V population does not under the conditions studied, and therefore one might consider using these ions in an attempt to detect nonequilibrium behaviour. Similarly, at higher temperatures one might use

ratios between different ions of Fe, one of relatively low charge state and another of higher charge state.

Additionally, one could look for observational signatures of the theoretically predicted emission spike seen at footpoint temperatures in simulation B (Fig. 10), particularly under conditions more severe than those presented here where it would be enhanced. Given that no such spike is evident in simulation A it might act as a signature for the presence of nonequilibrium ionisation by indicating an over-abundance of low-temperature emitters.

In the near future we plan to extend the work presented in the current paper in order to study higher energy phenomena such as microflares and flares, where we expect nonequilibrium effects to be considerably more pronounced and a nonequilibrium treatment of the radiative response of the plasma to be very important. This is particularly true of fast flows carrying material along a strong temperature gradient and in the radiative cooling phase of strongly heated, high temperature plasma. We wish to identify potential signatures of nonequilibrium ionisation in our theoretical models that will be of use in observational data analysis in order to ensure that observations are interpreted correctly and invalid assumptions in spectroscopic diagnostics are avoided. In addition we will continue our investigations into the viability of a nanoflare heating model to explain the high temperatures reached in the X-ray corona as the simulations we have presented here show promise in this direction.

Acknowledgements. SJB would like to thank Dr. G. Del-Zanna and Prof. N. Ljepojevic for helpful discussions during the research and code development undertaken for this paper. SJB thanks the University of Exeter, UK, for the allocation of computing time on their Saturn cluster which carried out one of the simulations described in the current paper. SJB thanks PPARC for the provision of a PhD studentship and their continued support throughout its duration. HEM acknowledges financial support from PPARC. Finally, we thank Dr. D. Spadaro for refereeing this paper and for the helpful comments and suggestions he made.

References

- Betta, R., Peres, G., Reale, F., & Serio, S. 1997, *A&AS*, 122, 585
 Borrini, G., & Noci, G. 1982, *Sol. Phys.*, 77, 153
 Bradshaw, S. J., & Mason, H. E. 2003, *A&A*, 401, 699
 Del-Zanna, G., & Mason, H. E. 2003, *A&A*, submitted
 Doschek, G. A., & Tanaka, K. 1987, *ApJ*, 323, 799
 Dupree, A. K., Moore, R., & Shapiro, P. R. 1979, *ApJ*, 229, L101
 Edgar, R. J., & Esser, R. 2000, *ApJ*, 538, L167
 Erdélyi, R., Sarro, L. M., & Doyle, J. G. 1998, *Proc. Solar Jets and Coronal Plumes*, ESA SP-421, 207
 Erdélyi, R., & Sarro, L. M. 1999, *Proc. 8th SOHO Workshop*, ESA SP-446, 299
 Feldman, U. 1992, *Phys. Scr.*, 46, 202
 Klimchuk, J. A., Antiochos, S. K., & Mariska, J. T. 1987, *ApJ*, 320, 409
 MacNeice, P. J., McWhirter, R. W. P., Spicer, D. S., & Burgess, A. 1984, *Sol. Phys.*, 90, 357
 MacNeice, P. 1986, *Sol. Phys.*, 103, 47
 Mason, H. E., & Monsignori Fossi, B. C. 1994, *A&ARv*, 6, 123
 Mazzotta, P., Mazzitelli, G., Colafrancesco, S., & Vittorio, N. 1998, *A&AS*, 133, 403
 Noci, G., Spadaro, D., Zappala, R., & Antiochos, S. K. 1989, *ApJ*, 338, 1131
 O'Shea, E., Banerjee, D., Doyle, J. G., Fleck, B., & Murtagh, F. 2001, *A&A*, 368, 1095
 Parker, E. N. 1988, *ApJ*, 330, 474
 Reale, F., Peres, G., Serio, S., Betta, R. M., DeLuca, E. E., & Golub, L. 2000, *ApJ*, 535, 423
 Sarro, L. M., Erdélyi, R., Doyle, J. G., & Pérez, M. E. 1999, *A&A*, 351, 721
 Serio, S., Peres, G., Vaiana, G. S., Golub, L., & Rosner, R. 1981, *ApJ*, 243, 288
 Spadaro, D., Zappala, R. A., Antiochos, S. K., Lanzafame, G., & Noci, G. 1990, *ApJ*, 362, 370
 Spadaro, D., Leto, P., & Antiochos, S. K. 1994a, *ApJ*, 427, 453
 Spadaro, D., Leto, P., & Antiochos, S. K. 1994b, *Space Sci. Rev.*, 70, 207
 Spadaro, D., Lanza, A. F., Lanzafame, A. C., et al. 2002, *Proc. SOHO 11 Symp.*, ESA SP-508, 331
 Spadaro, D., Lanza, A. F., Lanzafame, A., et al. 2003, *ApJ*, 582, 486
 Teriaca, L., Banerjee, D., Doyle, J. G., & Erdélyi, R. 1999a, *Proc. 8th SOHO Workshop*, ESA SP-446, 645
 Teriaca, L., Doyle, J. G., Erdélyi, R., & Sarro, L. M. 1999b, *A&A*, 352, L99
 Teriaca, L., & Doyle, J. G. 2001, *The Dynamic Sun. Proc. of the Summerschool and Workshop held at the Kanzelhöhe Solar Observatory*, ed. A. Hanslmeier, M. Messerotti, & A. Veronig (Kluwer Academic Publishers), ISBN 0-7923-6915-7, 307
 Young, P. R., Del-Zanna, G., Landi, E., et al. 2003, *A&AS*, 144, 135

Online Material

Appendix A

In this Appendix we present the results from a number of tests designed to assess the stability and the accuracy of our hydrodynamic code. The first test checks the stability of the numerical methods by ensuring that the initial equilibrium solution can be maintained in a steady-state for time-scales far longer than those of the impulsive events studied here. The second test is intended to check that the adaptive regridding scheme is working correctly by making sure that the steep gradients are tracked as they move and remain well resolved. The final test examines the accuracy and the convergence of the solutions obtained by repeating the first 100 s of the simulation with a stricter limit on the fractional variation in the widths of adjacent cells to obtain higher resolution.

Test 1: Fig. 11 shows temperature and density profiles along the whole loop (top two panels) and an enlarged view of the footpoint region (bottom two panels). The initial equilibrium solution was used and only the quiescent background heating term used to derive it was applied. The profiles are plotted at 0 s, 600 s, 1200 s and 1800 s of loop evolution. Clearly there are no significant changes in the profiles at all. The residual velocities are on the order of 100 m s^{-1} , which is several orders of magnitude less than the local sound speed, and they are seen to have no effect on the evolution of the plasma. Figure 11 also shows that the position of the steep transition region remains extremely steady and exhibits no unphysical diffusion or the slippage/oscillations back and forth along the coordinate axis that can occur.

Test 2: Fig. 12 shows temperature profiles in the footpoint region with the actual grid points plotted. At 50 s (diamonds) the conduction front hasn't quite reached the lower transition region and so the temperature profile remains in equilibrium. At 100 s (crosses) strong heating of what was initially chromospheric plasma to transition region temperatures has occurred and the transition region has moved further down the loop. The density of grid points at 100 s shows that the adaptive regridding scheme has been successful in tracking the transition region and ensuring that sufficient grid points are present to resolve it.

Test 3: Fig. 13 shows two sets of equivalent plots that differ only in the fractional variation in the widths of adjacent cells, which is limited to 0.1 in the top two panels and 0.05 in the bottom two panels. The density of grid points in the bottom two panels is greater than in the top two panels in regions of steep gradients and so the resolution is higher in the bottom two panels. This allows us to check the convergence of our solutions, which is an important aspect to consider when attempting to assess their accuracy. When a solution has converged to the greatest accuracy the numerical methods employed will allow then there should be no discernible differences in the solution when the resolution is increased. There are no significant differences in the temperature and density profiles between the top and bottom panels of Fig. 13, indicating that our hydrocode has calculated solutions that converge satisfactorily.

Our hydrocode appears to satisfy the conditions of stability, convergence and accuracy to an appropriate degree, while the adaptive regridding scheme ensures that the steep gradients

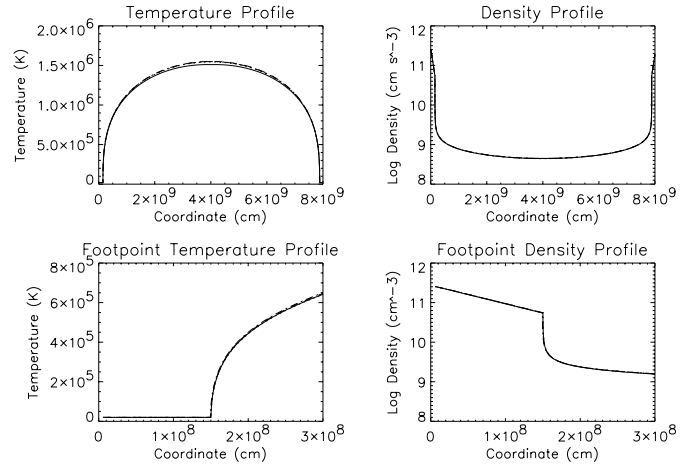


Fig. 11. Time series of the temperature and density along the loop (top two panels) and in the footpoint region (bottom two panels) as the initial solution is held in equilibrium with only the background heating term applied. The profiles are taken at: 0 s (solid line), 600 s (dotted), 1200 s (dashed), 1800 s (dash-dot).

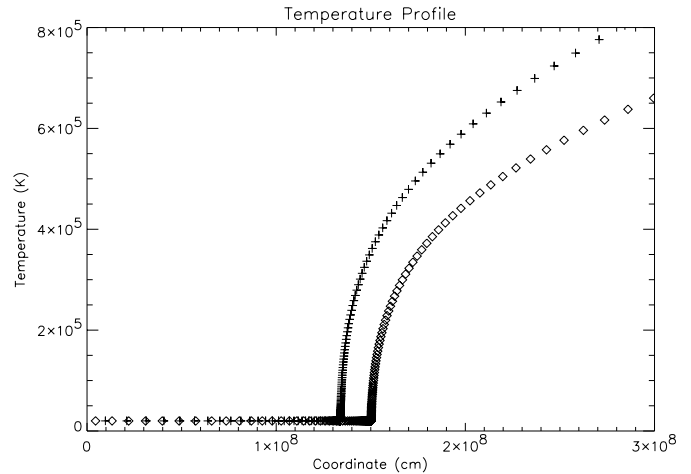


Fig. 12. Time series of temperature in the footpoint region of the loop with the grid points plotted. At 50 s (diamonds) the conduction front hasn't reached the lower transition region, whereas at 100 s (crosses) strong heating of the lower transition region and chromospheric plasma has occurred. The density of grid points at 100 s shows that the adaptive regridding scheme has been successful in tracking and adequately resolving the moving transition region.

encountered are successfully tracked and remain adequately resolved at all times.

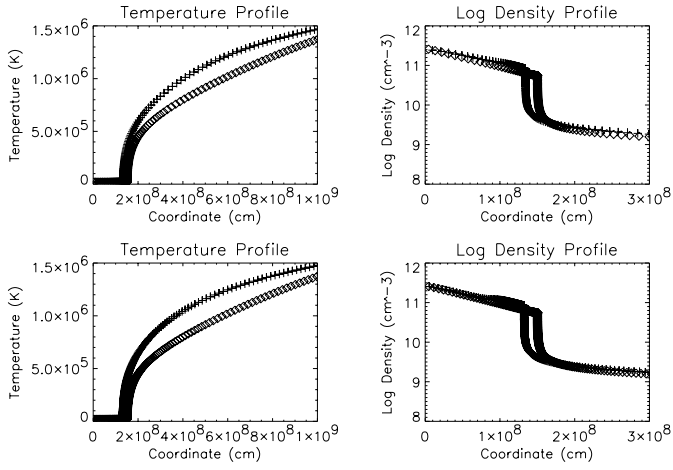


Fig. 13. Time series of temperature and density in the lower part of the loop with the grid points plotted. At 50 s (diamonds) the conduction front hasn't reached the lower transition region, whereas at 100 s (crosses) strong heating of the lower transition region and chromospheric plasma has occurred. The fractional variation in the widths of adjacent cells is limited to 0.1 in the top two panels and 0.05 in the bottom two panels.